Volume 11
Number 3
21 January 2023
Pages 761–1212

Journal of Materials Chemistry C

Materials for optical, magnetic and electronic devices

rsc.li/materials-c

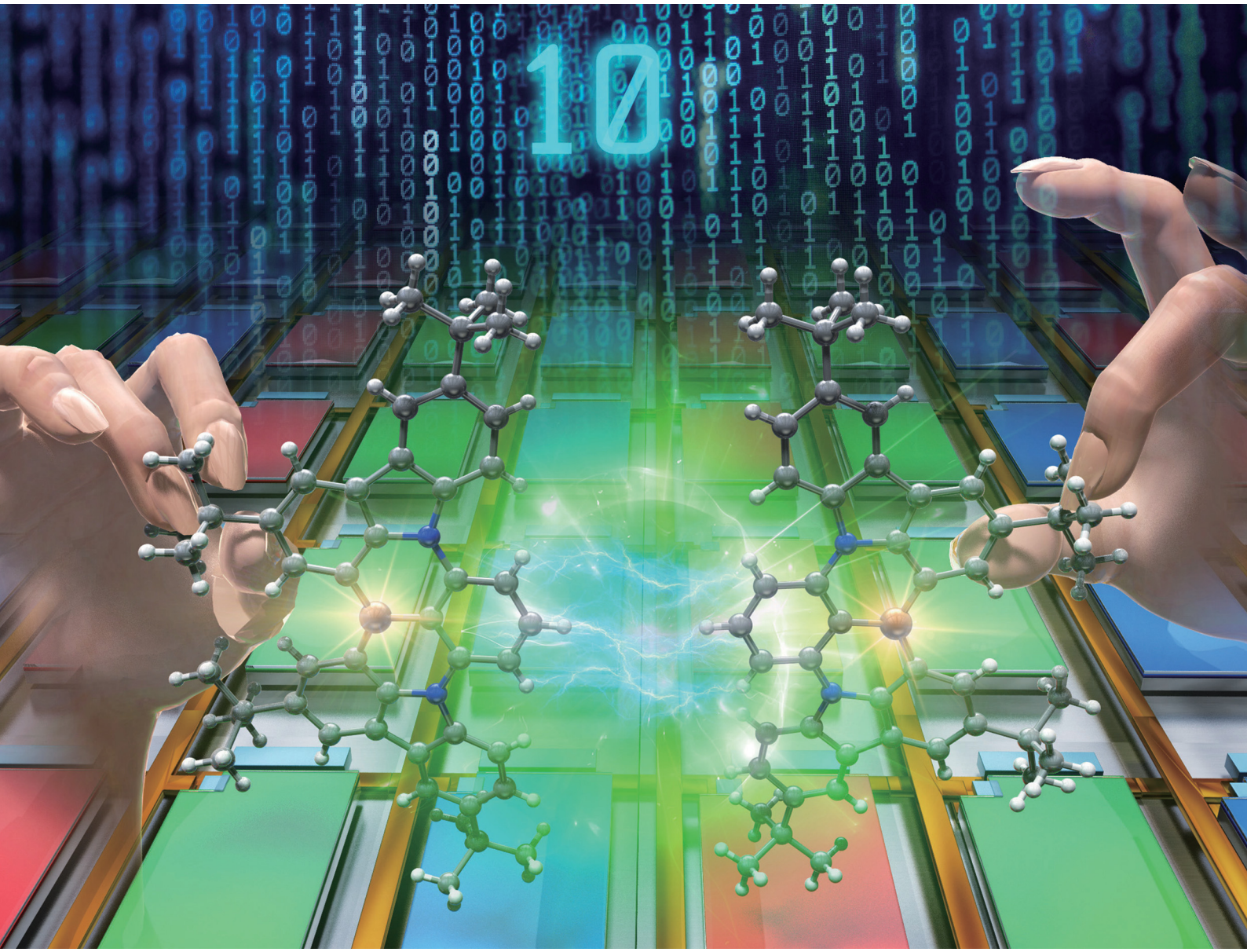

ISSN 2050-7526

ROYAL SOCIETY OF CHEMISTRY

PAPER
Takuma Yasuda *et al.*
Facile dimerization strategy for producing narrowband green multi-resonance delayed fluorescence emitters

10 YEARS ANNIVERSARY

Journal of Materials Chemistry C

ROYAL SOCIETY OF CHEMISTRY

PAPER

View Article Online
View Journal | View Issue

Cite this: J. Mater. Chem. C, 2023, 11, 917

Facile dimerization strategy for producing narrowband green multi-resonance delayed fluorescence emitters†

Minlang Yang,‡[a] Rajendra Kumar Konidena,‡[b] So Shikita[a] and Takuma Yasuda *[ab]

Received 19th October 2022,
Accepted 29th November 2022

DOI: 10.1039/d2tc04447a

rsc.li/materials-c

Establishing a simple molecular design strategy for enabling redshifted emissions while maintaining high color purity in multi-resonance thermally activated delayed fluorescence (MR-TADF) remains a crucial yet challenging task. Herein, we introduce a new design concept based on a dimerization strategy for constructing pure green MR-TADF emitters. Two isomeric MR dimers, namely ***p*-CzB** and ***m*-CzB**, were developed by tethering two MR fragments through different linking positions. The interconnection mode between the two MR fragments in these dimeric MR-TADF systems plays a vital role in regulating photophysical properties as well as exciton dynamics. Comprehensive photophysical and computational studies revealed that ***m*-CzB** exhibits superior green MR-TADF characteristics compared to ***p*-CzB**. A ***m*-CzB**-based organic light-emitting diode (OLED) delivered pure green electroluminescence with CIE coordinates of (0.20, 0.70), a maximum external quantum efficiency of 23.5%, and alleviated efficiency roll-off.

Introduction

Boron- and nitrogen-embedded polycyclic aromatic hydrocarbons (B,N-PAHs) have recently attracted burgeoning interest,[1–9] which is ascribable to their promising use in optoelectronic devices as typified by organic light-emitting diodes (OLEDs). The opposite resonance characteristics of mutually *ortho*-disposed B and N atoms in B,N-PAHs are capable of inducing the multiple-resonance (MR) effect, leading to the localization and separation of the highest occupied molecular orbital (HOMO) and lowest unoccupied molecular orbital (LUMO) on different constituent atoms.[5,6] This MR feature endows B,N-PAHs with a small singlet–triplet energy gap (ΔE_{ST}) and thermally activated delayed fluorescence (TADF) properties as a consequence.[4–9] The biggest advantage of such an MR-TADF emitter is its narrowband emission capability, with an extremely small full width at half maximum (FWHM < 40 nm) enabled by suppressing structural relaxation and vibronic coupling in excited states. Combining the capabilities of full exciton use and narrowband emission leads to ideal emitters for OLED applications, with superior electroluminescence (EL) efficiencies and color purities.

Three ultrapure red, green, and blue (RGB) primary emitters are essential for realizing wide-color-gamut OLEDs for use in ultrahigh-definition displays. The advent of sophisticated MR-TADF emitters, as represented by ν-DABNA, has led to the realization of high-efficiency pure blue EL.[6,10–15] However, owing to atomically separated HOMOs and LUMOs, these MR-TADF emitters typically possess feeble intramolecular long-range charge-transfer (CT) characteristics; hence, large bathochromic shifts from the blue emission-band region are difficult to achieve. Therefore, new viable design strategies that expand the color gamut of MR-TADF emitters beyond the blue region are in strong demand. In this regard, we focused on **BBCz-SB**[8,16] (Fig. 1) as one of the simplest B,N-based MR frameworks. Peripherally decorating **BBCz-SB** with either auxiliary donor or acceptor substituents on HOMO- or LUMO-dominant carbons has been reported to stabilize the respective energy levels, resulting in bathochromically shifted emissions.[17–23] Our group reported the first deep-red MR-TADF emitter featuring a large fused polycyclic π-system based on *para*-B-π-B and *para*-N-π-N conjugation.[8] High-efficiency green MR-TADF emitters have recently been developed by extending π-systems *via* additional ring fusion.[9,24–27]

Herein, we unveiled a simple but effective dimerization strategy for producing pure green MR-TADF emitters. Two isomeric MR dimers, namely ***p*-CzB** and ***m*-CzB**, were designed

[a] Department of Applied Chemistry, Graduate School of Engineering, Kyushu University, Fukuoka, Japan. E-mail: yasuda@ifrc.kyushu-u.ac.jp
[b] Institute for Advanced Study, Kyushu University, Fukuoka, Japan

† Electronic supplementary information (ESI) available. See DOI: https://doi.org/10.1039/d2tc04447a

‡ These authors contributed equally.

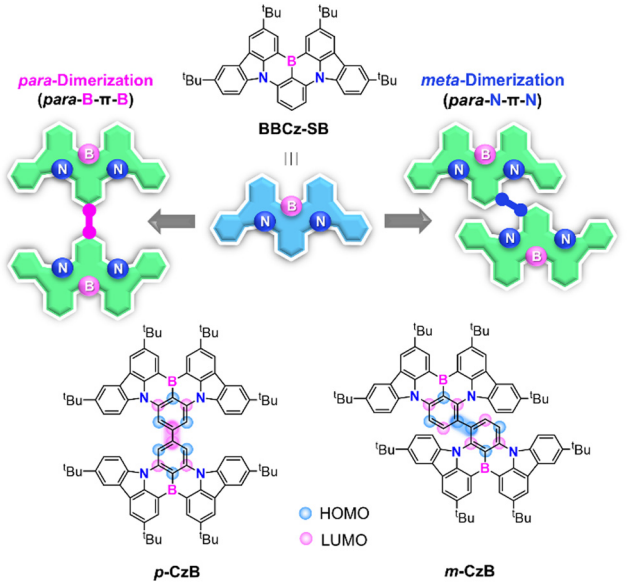

Fig. 1 Design of green MR-TADF emitters, ***p*-CzB** and ***m*-CzB**, based on the dimerization strategy.

by tethering two **BBCz-SB** fragments through different linking positions (Fig. 1). This dimerization strategy enables π-systems to be extended while maintaining intrinsic MR characteristics, thereby facilitating conspicuous bathochromic emission-band shifts without compromising narrowband spectral features. The dimerization strategy has previously been proposed for the design of TADF emitters;[28,29] however, narrowband emissions with an adequately small FWHM have not been achieved owing to their strong CT character. Indeed, ***p*-CzB** and ***m*-CzB** exhibited intense green photoluminescence (PL) emissions that peak at 505 and 515 nm in solution, with narrow FWHMs of 34 and 35 nm, respectively. Furthermore, an OLED based on ***m*-CzB** as the MR-TADF emitter displayed pure green EL with a high maximum external quantum efficiency (EQE_{max}) of 23.5% and high color purity.

Results and discussion

Scheme 1 outlines the route used to synthesize the dimeric MR-TADF emitters; detailed synthesis procedures and

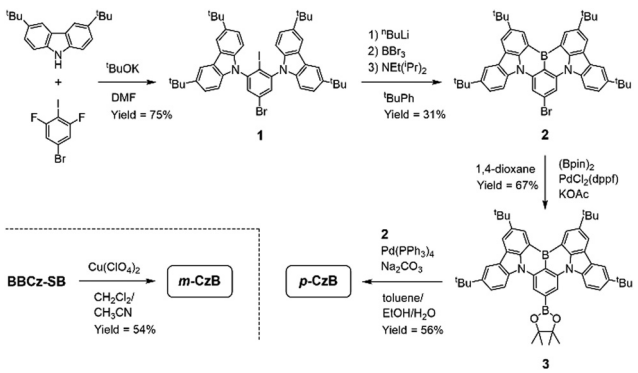

Scheme 1 Synthetic Routes to ***p*-CzB** and ***m*-CzB**.

characterization data are provided in the ESI.† The *para*-linked isomer (***p*-CzB**) was finally prepared in 56% yield by Suzuki–Miyaura cross-coupling between precursors **2** and **3**. Meanwhile, the *meta*-linked isomer (***m*-CzB**) was synthesized in 54% yield by the oxidative coupling of **BBCz-SB** using $Cu(ClO_4)_2{\cdot}6H_2O$ as the oxidant.[30] Since the HOMO of **BBCz-SB** is largely distributed on the *para*- and *ortho*-carbons of the central benzene ring with respect to the *N*-carbazolyl substituents,[8] oxidative coupling proceeded preferentially at this position to afford ***m*-CzB** in high yield. ***m*-CzB** has a distorted helicene-like structure with a *para*-N-π-N conjugated linkage. In addition, both dimeric ***p*-CzB** and ***m*-CzB** were found to be highly thermally stable with 5%-weight-loss decomposition temperatures (T_d) of 522 and 511 °C, respectively (ESI†), which are much higher than that of monomeric **BBCz-SB** (T_d = 411 °C).[8] The final products were purified by vacuum sublimation for subsequent use.

The photophysical properties of ***p*-CzB** and ***m*-CzB** were investigated as dilute toluene solutions and doped thin films, the results of which are shown in Fig. 2, with relevant photophysical data summarized in Table 1. Both ***p*-CzB** and ***m*-CzB** exhibit vivid green PL in solution, with emission peaks (λ_{PL}) at 504 and 515 nm, respectively, which are redshifted by 15–26 nm compared to that of **BBCz-SB** (λ_{PL} = 489 nm). Despite each dimeric structure being linked through a single bond, ***p*-CzB** and ***m*-CzB** exhibited small Stokes shifts of 28 and 27 nm and emission FWHMs of 34 and 35 nm, respectively, suggestive of miniscule geometrical changes in their excited states. ***m*-CzB** has a higher molar absorptivity (ε) than ***p*-CzB**, corresponding to a stronger MR-induced HOMO → LUMO transition. This trend eventually resulted in ***m*-CzB** exhibiting a higher PL quantum yield (Φ_{PL} = 90%) than ***p*-CzB** (Φ_{PL} = 85%) in solution. Solid thin films of ***p*-CzB** and ***m*-CzB** embedded in mCBP-CN[31] (3,3′-di(carbazol-9-yl)-5-cyano-1,1′-biphenyl), a bipolar host, showed narrowband green PL emissions with λ_{PL} = 513 and 517 nm, and Φ_{PL} = 80% and 85%, respectively (Fig. 2c, Table 1, and ESI†). The S_1 and T_1 excitation energies (E_S/E_T) of ***p*-CzB** and ***m*-CzB** were determined to be 2.43/2.29 and 2.40/2.31 eV, respectively, based on the peak wavelengths of their fluorescence and phosphorescence spectra (ESI†). Accordingly, ***m*-CzB** exhibited a smaller ΔE_{ST} than ***p*-CzB** (0.09 *vs.* 0.14 eV). Moreover, ***p*-CzB** underwent serious aggregation-caused emission quenching (ACQ) in the doped films with increasing the dopant concentration, whereas sterically distorted ***m*-CzB** exhibited slightly reduced ACQ effect, resulting in higher Φ_{PL} values (ESI†).

The transient PL decay profiles of the doped films of ***p*-CzB** and ***m*-CzB** show distinct two-component emissions (Fig. 2d). The prompt and delayed fluorescence lifetimes (τ_p/τ_d) were determined to be 9.6 ns/32 μs for ***p*-CzB** and 5.6 ns/15 μs for ***m*-CzB**. Benefiting from their prominent MR electronic features, both materials exhibited radiative decay rates (k_r) that far exceed 10^7 s^{-1}. Moreover, ***m*-CzB** (with the smaller ΔE_{ST}) exhibited a shorter τ_d, resulting in a k_{RISC} of 2.3 × 10^5 s^{-1} (Table 1), which is three-times higher than that of ***p*-CzB** (k_{RISC} = 4.7 × 10^4 s^{-1}). Notably, the k_{RISC} value of ***m*-CzB** is a

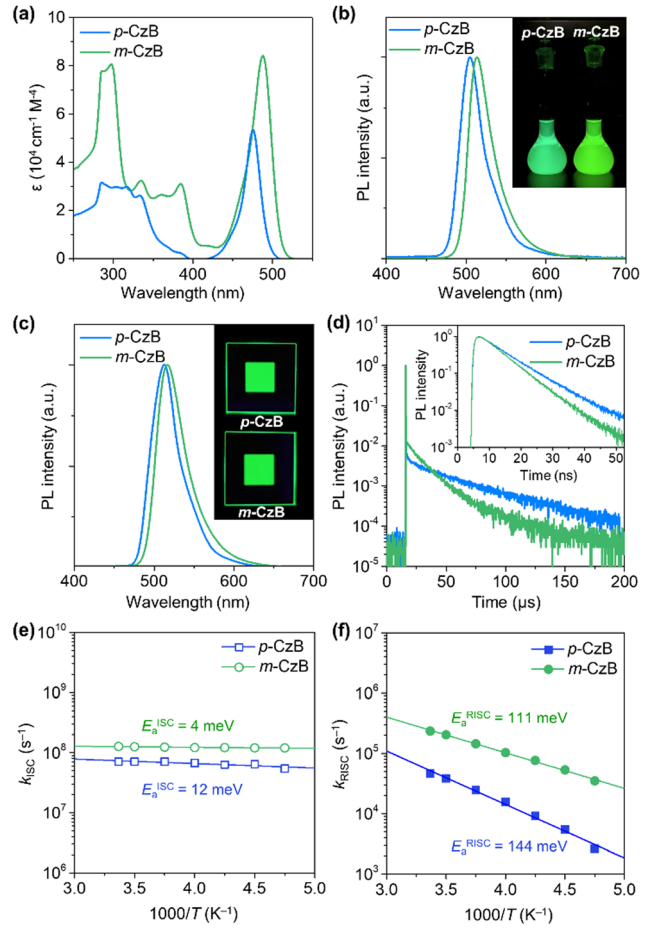

Fig. 2 (a) UV-vis absorption and (b) PL spectra of ***p*-CzBB** and ***m*-CzBB** in deoxygenated toluene (10^{-5} M) with a photographic image showing green emissions when illuminated by UV light (365 nm). (c) Steady-state PL spectra with corresponding emission images and (d) transient PL decay profiles acquired at 300 K for the doped films of ***p*-CzBB** and ***m*-CzBB** in mCBP-CN host matrices at a doping concentration of 1 wt%. The inset in (d) shows transient PL in the nanosecond (0–50 ns) region. (e and f) Arrhenius plots of k_{ISC} and k_{RISC} measured with the 1 wt%-emitter: mCBP-CN doped films, in which the solid lines represent the least-squares fittings for determining E_a^{ISC} and E_a^{RISC}.

standout among reported green MR-TADF emitters (ESI†). To further understand exciton thermodynamic behavior, we examined the temperature dependences of k_{ISC} and k_{RISC} for the doped films and determined the activation energies for ISC (E_a^{ISC}) and RISC (E_a^{RISC}) by fitting with the Arrhenius equation (Fig. 2e and f). While k_{ISC} showed negligibly small temperature dependences, k_{RISC} demonstrated clear positive temperature dependences, to give E_a^{RISC} values of 144 and 111 meV for ***p*-CzBB** and ***m*-CzBB**, respectively, which are in reasonable agreement with the foregoing ΔE_{ST} values. These results support the notion that the smaller ΔE_{ST} of ***m*-CzBB** accounts for its faster RISC.

To gain deeper insight into the nature of the excited singlet and triplet states, ***p*-CzBB** and ***m*-CzBB** were subjected to natural transition orbital (NTO) analyses using time-dependent density functional theory (TD-DFT) at the B3LYP/DZP level (Fig. 3). ***p*-CzBB** has quasi-degenerate highest occupied NTOs that reflect its symmetrical dimeric structure, where hole wave functions reside on different B/N-based MR cores and give rise to doubly degenerate singlet (S_1 and S_2) and triplet (T_1 and T_2) excited states (Fig. 3a). In this case, the electron wave functions are located across the two MR cores through *para*-*B*-π-B conjugation. Meanwhile, ***m*-CzBB** (with *para*-N-π-N conjugation) has degenerate lowest unoccupied NTOs; consequently, the electron wave functions are distributed in each of the two MR cores, while hole wave functions are extended to the dimeric MR structure (Fig. 3b). It is worth noting that the linking position significantly affects the resulting dimeric π-conjugated system and excited-state electronic properties.

We next calculated the spin–orbit coupling (SOC) matrix elements ($\langle S_m|\hat{H}_{SOC}|T_n\rangle$), m = 1, 2 and n = 1–4) for ***p*-CzBB** and ***m*-CzBB** (Fig. 3). As predicted by the El-Sayed rule,[32] the SOC values for T_1–S_1 and T_2–S_2 couples with the same orbital occupations are rather small (0.13 and 0.12 cm^{-1} for ***p*-CzBB** and 0.04 and 0.03 cm^{-1} for ***m*-CzBB**) because of negligible changes in orbital angular momentum. In contrast, T_2–S_1 and T_1–S_2 couples exhibit distinctly larger SOC values that are ascribable to larger changes in orbital angular momentum (0.42 and 0.40 cm^{-1} for ***p*-CzBB** and 0.36 and 0.54 cm^{-1} for ***m*-CzBB**). We therefore envisage that such quasi-degenerate low-energy excited states induced by these dimeric MR structures contribute to SOC enhancement and offer additional T–S spin-flip channels for RISC.[33] Indeed, despite very similar ΔE_{ST} values, dimeric ***p*-CzBB** and ***m*-CzBB** exhibit RISC rates that are accelerated by factors of more than three and eight, respectively, compared to monomeric **BBCz-SB** (k_{RISC} = 1.4 × 10^4 s^{-1} in toluene).[8]

Table 1 Photophysical data

compound	state[a]	λ_{PL}[b] (nm)	FWHM[c] (nm/eV)	Φ_{PL}[d] (%)	Φ_p[e] (%)	Φ_d[e] (%)	τ_p[f] (ns)	τ_d[f] (μs)	k_r[g] (10^7 s^{-1})	k_{RISC}[h] (10^4 s^{-1})	E_S[i] (eV)	E_T[i] (eV)	ΔE_{ST}[j] (eV)
***p*-CzBB**	Sol	505	34/0.16	85	32	53	9.3	58	3.3	4.2	2.46	2.29	0.17
	Film	513	41/0.20	80	35	45	9.6	41	3.7	4.6	2.43	2.29	0.14
***m*-CzBB**	Sol	515	35/0.16	90	23	67	4.9	32	4.7	12	2.42	2.29	0.13
	Film	517	40/0.19	85	24	61	6.0	15	4.1	23	2.40	2.31	0.09

[a] Sol = deoxygenated toluene solution (10^{-5} M) at 300 K; film = 1 wt%-doped film in a mCBP-CN host matrix at 300 K under N_2. [b] PL emission maximum. [c] Full width at half maximum of the PL spectrum given in wavelength and energy. [d] Absolute PL quantum yield evaluated using an integrating sphere under N_2. [e] Fractional quantum yields for prompt fluorescence (Φ_p) and delayed fluorescence (Φ_d); $\Phi_p + \Phi_d = \Phi_{PL}$. [f] Emission lifetimes for prompt fluorescence (τ_p) and delayed fluorescence (τ_d). [g] Rate constant for fluorescence radiative decay ($S_1 \rightarrow S_0$): $k_r = \Phi_p/\tau_p$. [h] RISC rate constant ($T_1 \rightarrow S_1$): $k_{RISC} = \Phi_d/(k_{ISC}\cdot\tau_p\cdot\tau_d\cdot\Phi_p)$. [i] Lowest excited singlet (E_S) and triplet (E_T) energies determined from fluorescence and low-temperature phosphorescence spectral peaks for the doped films. [j] Singlet–triplet energy gap: $\Delta E_{ST} = E_S - E_T$.

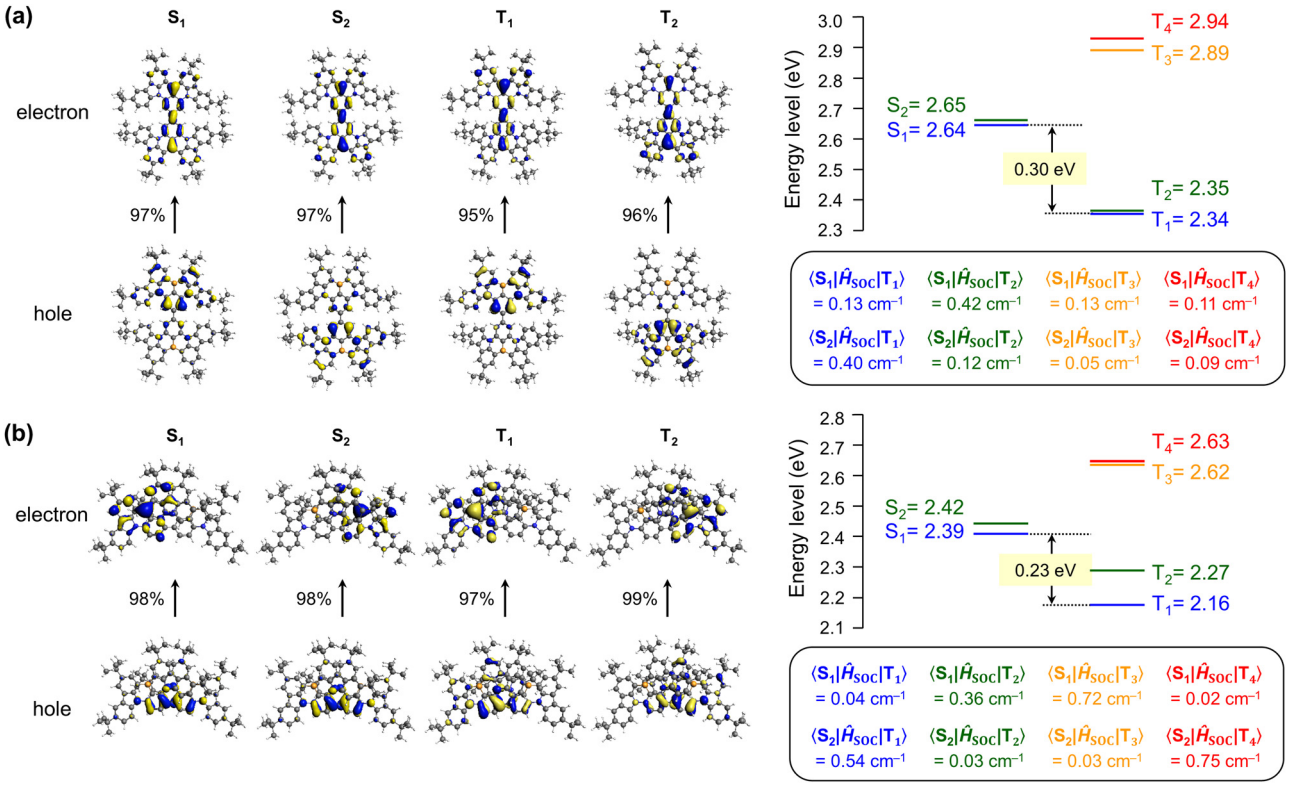

Fig. 3 Natural transition orbitals (NTOs) for the excited singlet (S_m) and triplet (T_n) states and simulated energy-level diagrams for (a) ***p*-CzB** and (b) ***m*-CzB**. NTOs, excitation energies for S_m and T_n, and associated spin–orbit coupling (SOC) matrix elements between the T_n and S_m states were calculated at the B3LYP/DZP level.

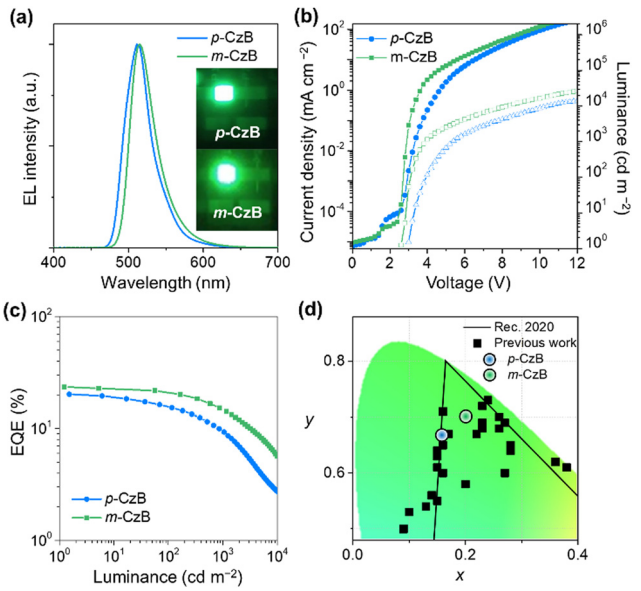

Fig. 4 EL characteristics of OLEDs that use ***p*-CzB** and ***m*-CzB** as MR-TADF emitters: (a) EL spectra and green EL images acquired at 10 mA cm^{-2}, (b) current density–voltage–luminance (J–V–L) characteristics, (c) EQE–L plots. (d) Comparing CIE coordinates for current and previously reported green OLEDs based on MR-TADF emitters (see ESI† for plotted data sets and source references).

Hence, the present dimerization strategy not only modulates the emission color but also favourably impacts excitonic spin conversion crucial for TADF.

To evaluate the actual EL performance of ***p*-CzB** and ***m*-CzB**, we tested TADF-OLEDs fabricated using the following device structure: indium-tin-oxide (ITO)/HAT-CN (10 nm)/TAPC (50 nm)/mMCP (5 nm)/1 wt%-emitter:mCBP-CN (30 nm)/PPF (5 nm)/B3PyPB (50 nm)/Liq (1 nm)/Al (100 nm);[13] the chemical structures of the materials are provided in the ESI.†Fig. 4 shows EL spectra, current density–voltage–luminance (J–V–L) characteristics, and EQE–L plots for the fabricated TADF-OLEDs, and relevant EL data are summarized in Table 2. TADF-OLEDs that incorporate ***p*-CzB** and ***m*-CzB** display narrowband green EL with emission peaks (λ_{EL}) at 511 and 515 nm and FWHMs of 41 and 39 nm, which correspond to CIE chromaticity coordinates of (0.16, 0.66) and (0.20, 0.70), respectively. Notably, the green EL color of the ***m*-CzB**-based device fulfils the requirements of the National Television System Committee (NTSC) for pure green (0.21, 0.71) and approaches the coordinates of Rec.2020 pure green (0.17, 0.79)[34] (Fig. 4d). Moreover, these OLEDs delivered high maximum EQEs of 20.2% and 23.5%, respectively (Fig. 4c and Table 2). It is worth noting that the ***m*-CzB**-based device showed a more alleviated efficiency roll-off and retained high EQEs of 21.0% and 15.0% at luminances of 100 and 1000 cd m^{-2}. The relatively high k_{RISC} of 2.3 × 10^5 s^{-1} for ***m*-CzB** accounts for the alleviated efficiency roll-off compared to that of ***p*-CzB** (4.6 × 10^4 s^{-1}) and contributes to suppressing

Table 2 OLED Performance

Emitter	*p*-CzB	*m*-CzB
V_{on}[a] (V)	3.2	2.8
λ_{EL}[b] (nm)	511	515
FWHM[c] (nm/eV)	41/0.20	39/0.19
CIE[d] (x, y)	(0.16, 0.66)	(0.20, 0.70)
EQE_{max}[e] (%)	20.2	23.5
$EQE_{100/1000}$[f] (%)	15.4/9.3	21.0/15.0
CE[g] (cd A^{-1})	67.9	85.1
PE[h] (lm W^{-1})	69.9	94.7

[a] Turn-on voltage at a luminance above 1 cd m^{-2}. [b] EL emission maximum at 10 mA cm^{-2}. [c] Full width at half maximum of the EL spectrum given in wavelength and energy. [d] Commisssion Internationale de l'Éclairage (CIE) chromaticity coordinates recorded at 10 mA cm^{-2}. [e] Maximum external EL quantum efficiency. [f] External EL quantum efficiencies at luminance of 100 and 1000 cd m^{-2}. [g] Maximum current efficiency. [h] Maximum power efficiency.

detrimental exciton quenching, such as triplet–triplet annihilation (TTA) in operation at high luminance. These different EL characteristics are also reflected in the operational stabilities of the TADF-OLEDs. The ***m*-CzB**-based device exhibited an operational lifetime with a 50% luminance reduction (LT_{50}) of 25.5 h at an initial luminance (L_0) of 100 cd m^{-2}, which is approximately four-times longer than that of the ***p*-CzB**-based device (LT_{50} = 6.4 h) (ESI†). These device stabilities sill leave much room for improvement; however, isomeric ***p*-CzB** and ***m*-CzB** reveal that a subtle difference in linking position can greatly impact the efficiency roll-off behavior and operational stability in OLEDs.

Conclusions

In summary, we introduced a facile dimerization strategy for producing narrowband green MR-TADF emitters. Based on this strategy, we developed *para*- and *meta*-linked isomeric MR dimers, ***p*-CzB** and ***m*-CzB**. The position connecting the two MR cores serves as a conjugation valve that regulates the photophysical properties of the emitter. Both ***p*-CzB** and ***m*-CzB** exhibited distinct MR-TADF characteristics, concurrently delivering pure green emissions and narrow spectral FWHMs. Notably, the color purity and k_{RISC} associated with the ***m*-CzB** emission are standouts among reported green MR-TADF emitters. Consequently, the ***m*-CzB**-based green OLED achieved a considerably high EQE_{max} of 23.5% as well as alleviated efficiency roll-off, outperforming the ***p*-CzB**-based device. We expect that these results will expediate new material designs that feature the dimerization strategy for constructing wide-color-gamut MR-TADF systems.

Author contributions

M. Y., R. K. K., and T. Y. conceptualized the project. M. Y. and S. S. synthesized materials and performed quantum chemical calculations. M. Y. performed photophysical analysis and device evaluations. M. Y., R. K. K., and T. Y. co-wrote the manuscript. T. Y. supervised the entire research project.

Conflicts of interest

There are no conflicts to declare.

Acknowledgements

This work was supported in part by Grant-in-Aid for JSPS KAKENHI (Grant No. JP21H04694 and JP22F21030), JST CREST (Grant No. JPMJCR21O5), and the Mitsubishi Foundation. R. K. K. acknowledges the JSPS Postdoctoral Fellowships for Research in Japan. The authors are grateful for the support provided by the Cooperative Research Program of "Network Joint Center for Materials and Devices" and the computer facilities at the Research Institute for Information Technology, Kyushu University.

References

1 M. Hirai, N. Tanaka, M. Sakai and S. Yamaguchi, *Chem. Rev.*, 2019, **119**, 8291–8331.
2 S. Oda and T. Hatakeyama, *Bull. Chem. Soc. Jpn.*, 2021, **94**, 950–960.
3 E. Von Grotthuss, A. John, T. Kaese and M. Wagner, *Asian J. Org. Chem.*, 2018, **7**, 37–53.
4 S. M. Suresh, D. Hall, D. Beljonne, Y. Olivier and E. Zysman-Colman, *Adv. Funct. Mater.*, 2020, **30**, 1908677.
5 T. Hatakeyama, K. Shiren, K. Nakajima, S. Nomura, S. Nakatsuka, K. Kinoshita, J. Ni, Y. Ono and T. Ikuta, *Adv. Mater.*, 2016, **28**, 2777–2781.
6 Y. Kondo, K. Yoshiura, S. Kitera, H. Nishi, S. Oda, H. Gotoh, Y. Sasada, M. Yanai and T. Hatakeyama, *Nat. Photonics*, 2019, **13**, 678–682.
7 K. Matsui, S. Oda, K. Yoshiura, K. Nakajima, N. Yasuda and T. Hatakeyama, *J. Am. Chem. Soc.*, 2018, **140**, 1195–1198.
8 M. Yang, I. S. Park and T. Yasuda, *J. Am. Chem. Soc.*, 2020, **142**, 19468–19472.
9 H. J. Kim and T. Yasuda, *Adv. Opt. Mater.*, 2022, **10**, 2201714.
10 C. Y. Chan, M. Tanaka, Y. T. Lee, Y. W. Wong, H. Nakanotani, T. Hatakeyama and C. Adachi, *Nat. Photonics*, 2021, **15**, 203–207.
11 S. O. Jeon, K. H. Lee, J. S. Kim, S. G. Ihn, Y. S. Chung, J. W. Kim, H. Lee, S. Kim, H. Choi and J. Y. Lee, *Nat. Photonics*, 2021, **15**, 208–215.
12 H. Tanaka, S. Oda, G. Ricci, H. Gotoh, K. Tabata, R. Kawasumi, D. Beljonne, Y. Olivier and T. Hatakeyama, *Angew. Chem., Int. Ed.*, 2021, **60**, 17910–17914.
13 I. S. Park, M. Yang, H. Shibata, N. Amanokura and T. Yasuda, *Adv. Mater.*, 2022, **34**, 2107951.
14 X. Lv, J. Miao, M. Liu, Q. Peng, C. Zhong, Y. Hu, X. Cao, H. Wu, Y. Yang, C. Zhou, J. Ma, Y. Zou and C. Yang, *Angew. Chem., Int. Ed.*, 2022, **61**, e2022015.
15 K. R. Naveen, H. Lee, R. Braveenth, K. J. Yang, S. J. Hwang and J. H. Kwon, *Chem. Eng. J.*, 2022, **432**, 134381–134388.
16 Y. Xu, Z. Cheng, Z. Li, B. Liang, J. Wang, J. Wei, Z. Zhang and Y. Wang, *Adv. Opt. Mater.*, 2020, **8**, 1902142.

17 Y. Zhang, D. Zhang, J. Wei, Z. Liu, Y. Lu and L. Duan, *Angew. Chem., Int. Ed.*, 2019, **58**, 16912.
18 Y. Xu, G. Li, Z. Li, Q. Wang, X. Cai, J. Wei and Y. Wang, *Angew. Chem., Int. Ed.*, 2020, **59**, 17442–17446.
19 Y. Qi, W. Ning, Y. Zou, X. Cao, S. Gong and C. Yang, *Adv. Funct. Mater.*, 2021, **31**, 2102017.
20 M. Yang, S. Shikita, H. Min, I. S. Park, H. Shibata and T. Yasuda, *Angew. Chem., Int. Ed.*, 2021, **60**, 23142–23147.
21 Y. Liu, X. Xiao, Y. Ran, Z. Bin and Y. You, *Chem. Sci.*, 2021, **12**, 9408–9412.
22 Y. Xu, C. Li, Z. Li, J. Wang, J. Xue, Q. Wang, X. Cai and Y. Wang, *CCS Chem.*, 2021, **4**, 2065–2079.
23 Y. Zhang, D. Zhang, T. Huang, A. J. Gillett, Y. Liu, D. Hu, L. Gui, Z. Bin, G. Li, J. Wei and L. Duan, *Angew. Chem., Int. Ed.*, 2021, **60**, 20498–20503.
24 Y. Zhang, D. Zhang, J. Wei, X. Hong, Y. Lu, D. Hu, G. Li, Z. Liu, Y. Chen and L. Duan, *Angew. Chem., Int. Ed.*, 2020, **59**, 17499–17503.
25 Y. Zhang, G. Li, L. Wang, T. Huang, J. Wei, G. Meng, X. Wang, X. Zeng, D. Zhang and L. Duan, *Angew. Chem., Int. Ed.*, 2022, **61**, e202202380.
26 X. F. Luo, H. X. Ni, H. L. Ma, Z. Z. Qu, J. Wang, Y. X. Zheng and J. L. Zuo, *Adv. Opt. Mater.*, 2022, **10**, 2102513.
27 Y. Xu, Q. Wang, J. Wei, X. Peng, J. Xue, Z. Wang, S. J. Su and Y. Wang, *Angew. Chem., Int. Ed.*, 2022, **61**, e202204652.
28 Y. J. Cho, S. K. Jeon, B. D. Chin, E. Yu and J. Y. Lee, *Angew. Chem., Int. Ed.*, 2015, **54**, 5201–5204.
29 D. Sun, S. M. Suresh, D. Hall, M. Zhang, C. Si, D. B. Cordes, A. M. Z. Slawin, Y. Olivier, X. Zhang and E. Zysman-Colman, *Mater. Chem. Front.*, 2020, **4**, 2018–2022.
30 S. Shikita, T. Harada and T. Yasuda, *Chem. Commun.*, 2022, **58**, 4849–4852.
31 S. G. Ihn, N. Lee, S. O. Jeon, M. Sim, H. Kang, Y. Jung, D. H. Huh, Y. K. Son, S. Y. Lee, M. Numata, H. Miyazaki, R. Góomez-Bombarelli, J. Aguilera-Iparraguirre, T. Hirzel, A. Aspuru-Guzik, S. Kim and S. Lee, *Adv. Sci.*, 2017, **4**, 1600502.
32 M. A. El-Sayed, *Acc. Chem. Res.*, 1968, **1**, 8–16.
33 H. Min, I. S. Park and T. Yasuda, *Adv. Opt. Mater.*, 2022, **10**, 2200290.
34 Recommendation ITU-R BT.2020: parameter values for ultrahigh definition television systems for production and international program exchange, International Telecommunication Union, 2012.

